

Electronic-Photonic Integrated Circuit for 3D Microimaging

Behnam Behroozpour, *Member, IEEE*, Phillip A. M. Sandborn, Niels Quack, *Senior Member, IEEE*, Tae-Joon Seok, *Member, IEEE*, Yasuhiro Matsui, Ming C. Wu, *Fellow, IEEE*, and Bernhard E. Boser, *Fellow, IEEE*

Abstract—An integrated electronic-photonic phase-locked loop (PLL) modulates the frequency of a tunable laser for use in frequency-modulated continuous-wave (FMCW) lidar 3D imaging. The proposed lidar can perform 180k range measurements per second. The rms depth precision is 8 μm at distances of $\pm 5 \text{ cm}$ from the range baseline. The range window is 1.4 m, with a precision of 4.2 mm at the edges of the window. Optical circuitry, including input light couplers, waveguides, and photodiodes, is realized on a 3 mm \times 3 mm silicon-photonic chip. The 0.18- μm CMOS ASIC of the same area comprises the front-end transimpedance amplifier, analog electro-optical PLL, and digital control circuitry consuming 1.7 mA from a 1.8 V supply and 14.1 mA from a 5-V supply. The latter includes 12.5-mA bias current for the distributed Bragg reflector section of the tunable laser. The two chips are integrated using through-silicon-vias implemented in the silicon-photonic chip.

Index Terms—3D imaging, 3D microimaging, coherent imaging, electronic-photonic integrated circuit, electro-optical phase-locked loop (EO-PLL), frequency-modulated continuous-wave (FMCW) lidar, heterogeneous integration, microranging, silicon photonic.

I. INTRODUCTION

MICRORANGING and 3D microimaging have key importance in industrial measurement systems. There are existing tools for this purpose, but their large form factors limit their usage to manufacturing industries. A chip-scale solution can make this technology accessible to a wider range of applications, such as introducing 3D-imaging capability to the modern 3D printers to create high-fidelity 3D copy machines. Many medical applications, including corneal imaging for contact lens fitting and 3D vision for robotic microsurgery, would benefit from this technology as well.

There are two main classes of 3D imaging technologies. The ones in the first category use image processing; these include stereovision [1], [2], structured-light cameras [3]–[5], and multifocus imaging [6]–[8]. These methods are based on

Manuscript received May 9, 2016; revised August 30, 2016; accepted October 14, 2016. Date of publication November 21, 2016; date of current version January 4, 2017. This paper was approved by Guest Editor Roman Genov.

B. Behroozpour was with the University of California, Berkeley, CA 94720 USA, and is currently with the Bosch Research and Technology Center, Palo Alto, CA 94304 USA (e-mail: behroozpour@berkeley.edu).

P. A. M. Sandborn, T.-J. Seok, M. C. Wu, and B. E. Boser are with the University of California at Berkeley, Berkeley, CA 94720 USA.

N. Quack was with the University of California, Berkeley, CA 94720 USA, and is currently with EPFL, 1015 Lausanne, Switzerland.

Y. Matsui is with Finisar Corporation, Fremont, CA 94538 USA.

Color versions of one or more of the figures in this paper are available online at <http://ieeexplore.ieee.org>.

Digital Object Identifier 10.1109/JSSC.2016.2621755

correlating the features on photographs of a scene, such as the view angle, curvature of the illumination pattern, or blur and gradient of focus, with the scene's 3D geometry. These image-processing techniques typically rely on mainstream hardware, including photographic cameras and processor chips, and are, therefore, suitable for inexpensive depth estimations. However, their dependence on features of optical pictures, such as object edges, makes them inaccurate for measuring distances to certain classes of objects, such as those with white shiny surfaces or smooth curvatures.

The second category of 3D imagers is based on measuring the round-trip delay of an ultrasonic or electromagnetic wave to the target. Ultrasonic rangefinders can operate with very low power consumption, making them suitable for detection and ranging in mobile devices [9], but their lateral and depth resolution are both limited by their millimeter-scale ultrasonic wavelengths. Ultrasonic waves with shorter wavelengths exhibit exponentially larger attenuation in air, rendering them impractical for high-precision 3D imaging. Radars and lidars use electromagnetic waves in radio and optical spectra, respectively. Light waves have much shorter wavelengths than RF waves; thus, lidars can offer better lateral resolution and depth precision than radars [10], making them more suitable for the aforementioned 3D microimaging applications.

The most straightforward lidar architecture is based on measuring the round-trip delay of a light pulse to the target [11], [12]. As shown in Fig. 1(a), this type of lidar consists of a pulsed light source (e.g., laser), a detector, and the electronic timing circuitry. The simplicity of the optical parts in a pulsed lidar makes it attractive for many applications. However, considering the timing diagram of Fig. 1(b), to achieve below 10- μm range precision, the electronic circuits must be able to measure the round-trip delay of the light pulse with a precision of approximately 70 fs. This is a difficult task for present-day electronic circuits, and toward this objective, frequency-modulated continuous-wave (FMCW) lidar [13]–[15] can relax the required precision in the round-trip delay measurement in exchange for a more sophisticated optical architecture.

One of the difficulties in implementing FMCW lidars is the precise modulation of the laser frequency. Previously, this task has been accomplished using bench-top devices [16], [17]. In this paper, we present an electronic-photonic integrated circuit for laser frequency modulation that demonstrates better precision than previously reported results from the bench-top systems and enables chip-scale 3D microimaging.

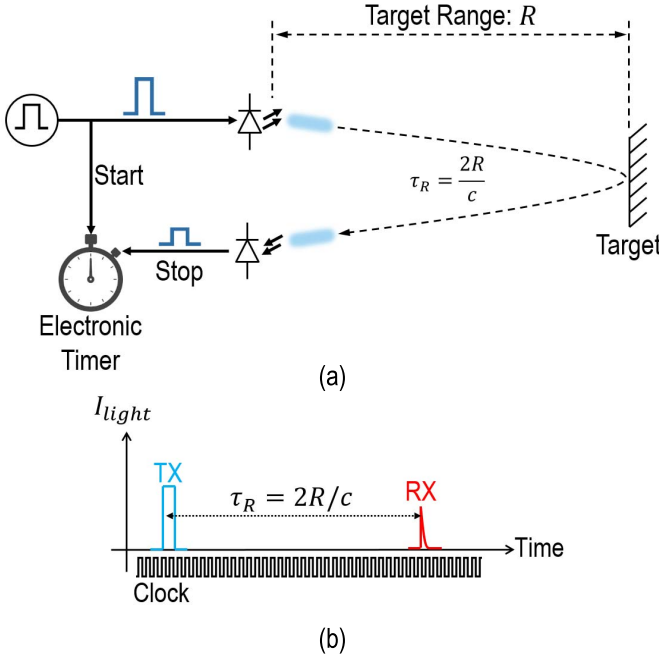


Fig. 1. Principle of operation for conventional pulsed lidar. (a) Architecture. (b) Waveform of the light intensity.

This paper is organized into seven sections. Section II presents the operating principle of the FMCW lidar. Sections III and IV describe the operation principle and the design procedure, respectively, of the electro-optical phase-locked loop (EO-PLL) proposed for laser frequency modulation. Practical aspects of the implementation, including simulation and fabrication, are discussed in Section V. Section VI shows the experimental setup and the measurement results. Section VII provides the conclusion.

II. FREQUENCY-MODULATED CONTINUOUS-WAVE LIDAR

Fig. 2(a) shows the architecture of the FMCW lidar, which basically consists of a tunable laser and a coherent receiver. The optical frequency of the laser is linearly modulated with time. The laser light hits the target, and its reflection is collected in the receiver and combined with a local branch of the laser light. As shown in Fig. 2(b), the time delay between the local light and the reflection causes a frequency difference between the two light signals. Consequently, a beat tone at the frequency equal to this difference appears on the interference of the two light beams and is detected by a photodiode. The target range R can be determined by measuring the beat frequency of the photocurrent f_R as follows:

$$f_R = \frac{2\gamma}{c} \cdot R \quad (1)$$

where γ is the slope of the laser frequency modulation and c is the speed of light in free space.

A. Required Timing Accuracy for FMCW Versus Pulsed Lidar

It was previously mentioned that the electronic timing precision required for microranging can be more relaxed for

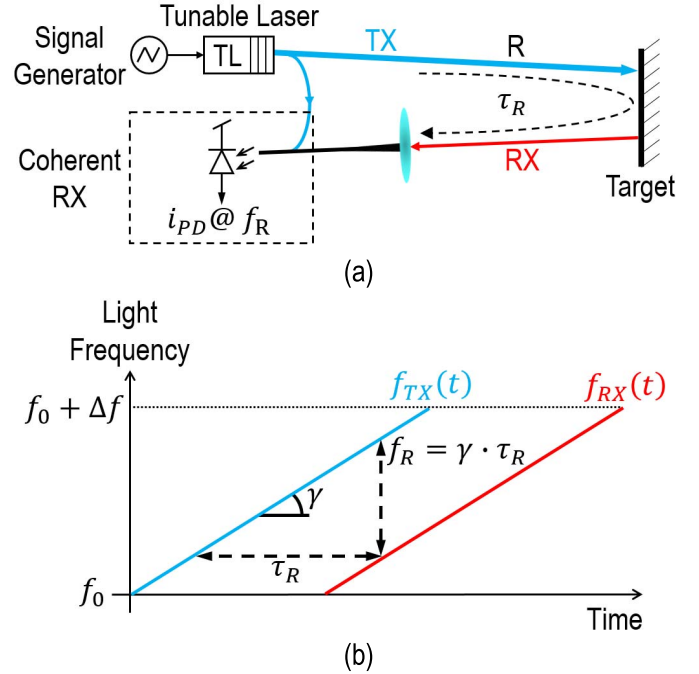


Fig. 2. Operation principle of FMCW lidar. (a) Architecture. (b) Waveform of the light frequency.

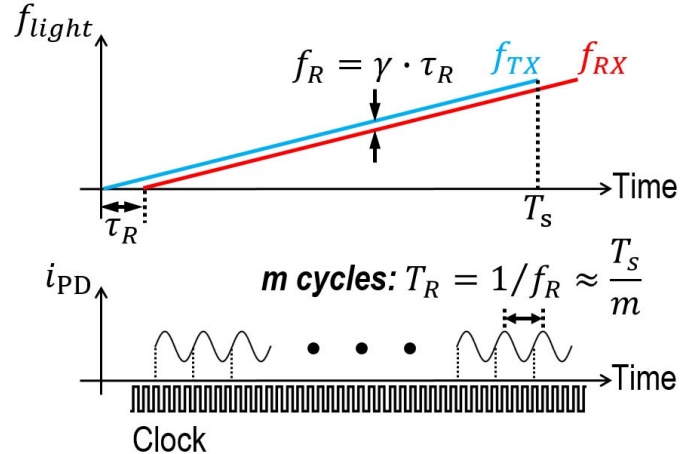


Fig. 3. FMCW lidar measurement with electronic clock.

an FMCW lidar compared with a pulsed one. In order to compare these two techniques, without loss of generality, it can be assumed that the best achievable timing precision for the measurement of the time-of-flight in a pulsed lidar and the period of the beat signal in an FMCW lidar is defined by the period of an electronic clock T_{clk} . In addition, for both cases, the sample time during which a single ranging measurement should be performed is equal to T_s . As shown in Fig. 1(b), in a pulsed lidar, the ranging precision can be found from the following equation:

$$\delta R = \frac{1}{2} c \cdot T_{clk}. \quad (2)$$

According to this equation, to achieve ranging precision below $10 \mu\text{m}$ using a pulsed lidar, the electronic circuitry should resolve the pulse time-of-flight with a precision of approximately 70 fs. For FMCW lidar, however, the situation is different. Consider the waveforms shown in Fig. 3. From (1),

the frequency of the beat signal is proportional to the target range. Assume that for a particular range R , the beat tone has m cycles within the sample time T_s . For a single range measurement, the timing error caused by the clock period will equally distribute among the m successive cycles of the beat signal. From (2), the ranging error can then be found as follows:

$$\begin{aligned}\delta R &= \delta f_R \cdot \frac{c}{2\gamma} = \frac{\delta T_R}{T_R} \cdot f_R \cdot \frac{c}{2\gamma} = \frac{\delta T_R}{T_R} \cdot R \\ &\approx \frac{T_{\text{clk}}/m}{T_s/m} \cdot R = \frac{T_{\text{clk}}}{T_s} \cdot R\end{aligned}\quad (3)$$

where $f_R \cdot (c/(2\gamma))$ is replaced by R using (1). It must be noted that T_R has been replaced by T_s/m just to find an estimate value for the error. As mentioned before, to perform a range measurement, a high-frequency clock can be used to acquire a more precise value of T_R . Based on (3), at a constant measurement rate set by T_s , the ranging error caused by the limited timing precision is proportional to the range R . Thus, for short ranges, FMCW lidar can provide a better ranging precision than a pulsed lidar. As an example, consider a ranging measurement at a rate of 1 MP/s for a target at a distance of 10 cm. Using (3), with an FMCW lidar, the required timing precision for the electronic circuits would be 100 ps, which is approximately 1400 times larger than the precision required for the pulsed lidar. From this discussion, the primary advantage of the FMCW lidar for high-precision range finding and 3D imaging is clear.

B. Laser Phase Noise and Photodiode Shot Noise

The phase noise of the tunable laser and the shot noise from the photodiode are the two primary limiting factors on the ranging precision and maximum operating distance of an FMCW lidar. In this part, a comprehensive analysis for the effect of these two noise sources on the performance of the FMCW lidar is presented.

1) Laser Phase Noise: The phase noise of the laser causes phase noise in the spectrum of the photocurrent in the coherent receiver. An analysis of this phenomenon is given in [18]. In that work, it is assumed that the laser's frequency noise has a white spectrum. This is a valid assumption for fixed-frequency lasers in which the majority of frequency noise is the result of spontaneous emissions in their active regions. However, for a tunable laser in which the noise is dominated by the contribution from the band-limited tuning process, a colored frequency noise spectrum must be assumed. The work presented in this paper uses an edge-emitting distributed Bragg reflector (DBR) laser with carrier-injection tuning and a central wavelength of approximately 1530 nm [19]. The schematic of the device with two electrical ports is shown in Fig. 4(a). The multiple quantum well gain section is biased at 40 mA, well above the threshold current to ensure the spontaneous emission noise in the gain section was suppressed. The lasing wavelength was tuned by the current injection into the DBR section, which changes the refractive index of the tuning section by the plasma effect of the free electrons. The tuning speed of DBR section is determined by the spontaneous emission lifetime of electron-hole pairs. As a

result, the transfer function from the tuning current to the laser frequency is a first-order low-pass filter with a bandwidth of $\omega_p = 2\pi \times 60$ Mrad/s. The average current in the tuning section is 12.5 mA, which results in a shot noise density of 4×10^{-21} A²/Hz. Through the 24-GHz/mA tuning gain, this value of shot noise translates into optical frequency noise level of $f_n^2 = 2.3 \times 10^6$ Hz²/Hz at dc.

For round-trip-delay to the target equal to τ_R and defining $\zeta_R = 1/(\pi^2 f_n^2 \omega_p^2 \tau_R^2)$, the spectral density of the photocurrent in an FMCW lidar employing this laser is derived as detailed in the Appendix, resulting in

$$\begin{aligned}S_i(\omega) &= \frac{i_0^2}{2} \left\{ e^{\frac{-2}{\zeta_R \cdot \omega_p}} \cdot \text{sinc}^2 \left(\frac{T_{\text{ramp}} \cdot \omega}{2} \right) + \frac{\zeta_R}{1 + (\zeta_R \omega_p / 2)^2} \right. \\ &\quad \left. \cdot \left[1 - e^{\frac{-2}{\zeta_R \cdot \omega_p}} \cdot \left(\cos \left(\frac{\omega}{\omega_p} \right) + \frac{1}{\zeta_R \cdot \omega} \cdot \sin \left(\frac{\omega}{\omega_p} \right) \right) \right] \right\}\end{aligned}\quad (4)$$

where the first term is the signal spectrum measured during a single modulation ramp, the second term is the noise spectrum, and i_0 is the amplitude of the sinusoidal photocurrent in the absence of the laser phase noise. By adding the detector shot noise to this spectrum, the signal-to-noise-ratio (SNR) in the receiver can be found.

2) Scattering Loss and Photodiode Shot Noise: The level of shot noise is determined from (5), based on the total average current in the detector I_D

$$i_{n-\text{shot}}^2 = 2q_e I_D = 2q_e [I_{\text{dark}} + R_{\text{PD}}(P_L + P_r)] \approx 2q_e R_{\text{PD}} P_L \quad (5)$$

where q_e is the electron charge, I_{dark} is its dark current, and R_{PD} is its responsivity; P_L is the optical power from the local branch in the coherent receiver and P_r is the optical power collected from the target reflection. In most cases, the photocurrent from the light in the local optical branch is dominant and the given approximation can be used. To compare the contribution of the laser phase noise and the detector shot noise, the amplitude of the photocurrent i_0 must be found. For a receiving aperture area of A_r , a target distance of R , and a reflectivity of α , and with the assumption of Lambertian scattering, the value of P_r can be found

$$P_r = \frac{\alpha \cdot A_r}{\pi R^2} \cdot P_t = \frac{\alpha \cdot A_r}{\pi \cdot c^2 \cdot \tau_R^2} \cdot P_t \quad (6)$$

where P_t is the transmitted power, and the photocurrent amplitude i_0 is given as follows:

$$i_0 = R_{\text{PD}} \sqrt{P_L \cdot P_r}. \quad (7)$$

Using this result and considering the near-carrier flat component of the noise spectrum in (4) and for $\tau_R^2 \ll (1/(4\pi\omega_p f_n^2))$ (i.e., target distance well within the coherent range of the laser), the spectral noise level caused by laser frequency noise can be approximated as follows:

$$\begin{aligned}i_{n-\text{Lpn}}^2 &= \frac{i_0^2}{4\omega_p} [1 - e^{-4\pi\omega_p f_n^2 \tau_R^2}] \text{sinc} \left(\frac{\omega}{\omega_p} \right) \\ &\approx \frac{4}{c^2} \alpha \cdot A_r \cdot R_{\text{PD}}^2 \cdot P_L \cdot P_t \cdot f_n^2.\end{aligned}\quad (8)$$

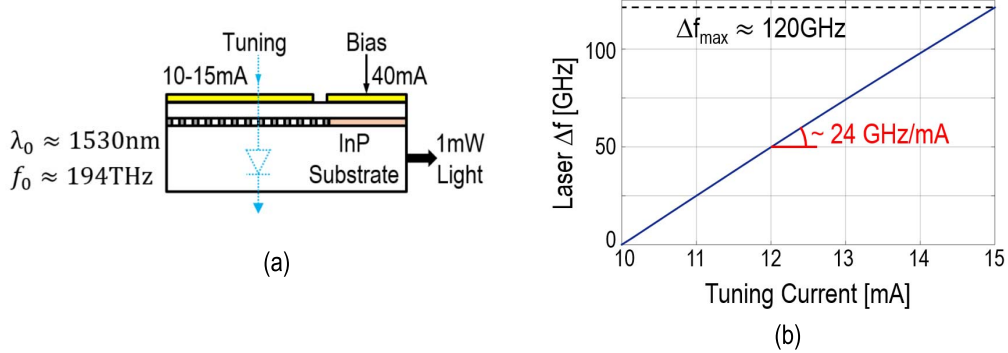


Fig. 4. Tunable DBR laser. (a) Schematic. (b) Frequency tuning characteristic.

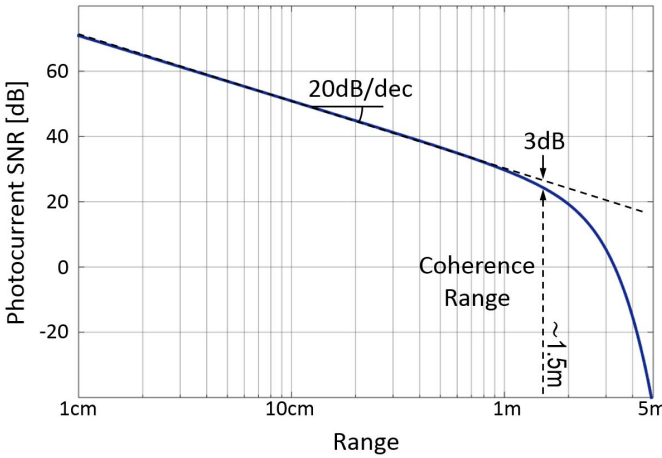


Fig. 5. SNR versus target range, R .

According to (5) and (8), under the following condition, the detector shot noise will be negligible:

$$\frac{2}{c^2} \alpha \cdot A_r \cdot R_{\text{PD}} \cdot P_t \cdot f_n^2 > q_e. \quad (9)$$

For $\alpha = 10\%$, $A_r \approx 1\text{in}^2$, and $R_{\text{PD}} = 0.8$, and with the laser used in this paper, the right-hand side of this inequality will evaluate to approximately $1.8 \times 10^{-18}\text{C}$, larger than $10 \times q_e$. Hence, in this paper, the laser phase noise will always be the limiting factor for the performance of the lidar.

Fig. 5 shows the value of the SNR versus the range R calculated numerically using (4) and (5). Using these equations and considering the postprocessing steps (e.g., filtering, sampling, and frequency measurement based on zero crossings of the signal), the ranging error versus the range is calculated and plotted in Fig. 6. It is important to note that unlike predictions generated by the assumption of a white frequency-noise spectrum [18], the rms value of the range error versus the range decreases at a rate much sharper than \sqrt{R} for closer targets. This result can be attributed to the colored spectrum of the laser frequency noise that causes better phase noise cancellation when mixing the local light signal and the reflection from a short-range target to generate the beat tone; on top of this, the particular postprocessing steps employed in this paper, such as decreasing the filtering bandwidth in digital domain for closer targets help to further improve the precision.

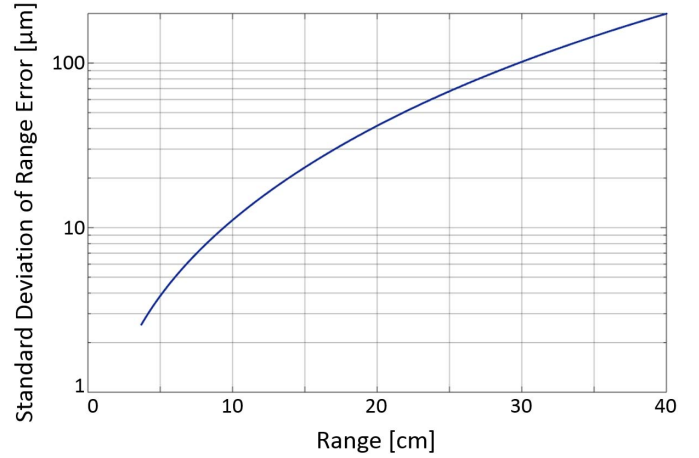


Fig. 6. Standard deviation of the ranging error, σ_R , versus range, R .

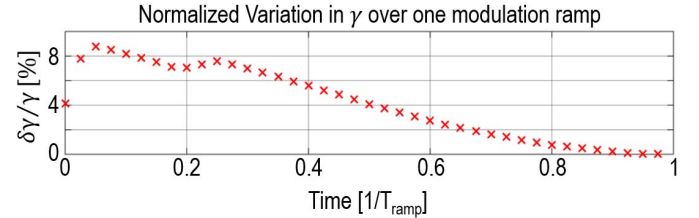


Fig. 7. Nonlinearity in the laser-tuning characteristic.

III. ELECTRO-OPTICAL PLL PRINCIPLE

It was previously mentioned that one of the important issues when employing a tunable laser in an FMCW lidar is the linearity of its frequency-tuning characteristic. Fig. 7 shows the modulation nonlinearity of the DBR laser used in this paper. In addition to this systematic variation that can be reduced by calibration, there is also random drift in the tuning characteristic. Measurement results indicate that this drift causes a 65-μm ranging error for a target placed at a distance of 5 cm. One way to suppress both the nonlinearity and the drift in the tuning characteristic is to use an EO-PLL [16].

A. Linear Frequency Modulation of the Laser Using Feedback

The basic architecture of an EO-PLL is shown in Fig. 8. The operation of this feedback mechanism can be more easily understood by first considering the subblocks enclosed in the

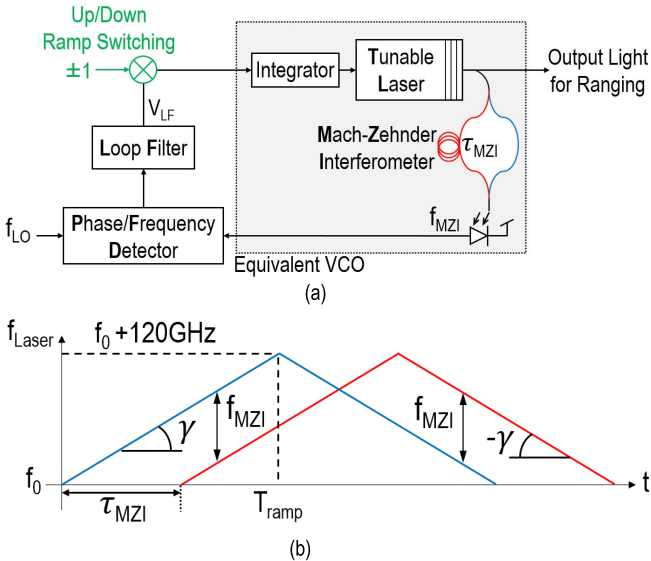


Fig. 8. EO-PLL for triangular frequency modulation of the laser light. (a) EO-PLL architecture. (b) Triangular waveform of the laser frequency.

dashed box. Assuming that a constant voltage is applied to the input of the integrator, its output would be a voltage ramp resulting in linear modulation of the laser frequency. With linear frequency modulation, the light will then propagate into the asymmetric Mach–Zehnder interferometer (MZI). As with the FMCW ranging measurement, the delay between the two light beams in the MZI arms creates a beat tone at its output. With fixed MZI delay, any variation in the MZI beat frequency is proportional to the deviation of the modulation slope, γ . The EO-PLL, similar to an electronic PLL, locks the beat frequency to a clean electronic local oscillator (LO) fixing the modulation slope γ to the following value:

$$\gamma = \frac{f_{LO}}{\tau_{MZI}} \quad (10)$$

where f_{LO} is the frequency of the electronic LO and τ_{MZI} is the differential delay of the MZI.

B. Switching Between Up and Down Ramps

The linear frequency modulation of the laser cannot continue indefinitely. The frequency of the DBR laser used in this paper can be tuned up to 120 GHz, and after that, it should either be reset or the modulation slope should be reversed to a down ramp. In this paper, the sign of the input signal to the integrator is periodically inverted to switch the modulation between up and down ramps, as shown in Fig. 8.

IV. EO-PLL DESIGN

In this section, a more rigorous analysis of the performance of the EO-PLL is presented, including loop gain and stability, modulation speed, and ramp-switching control.

A. Loop Gain and Stability

As previously mentioned, the slope of the laser frequency modulation should be reversed periodically. This switching process can cause a large disturbance in the MZI beat frequency and the EO-PLL should have sufficiently large locking

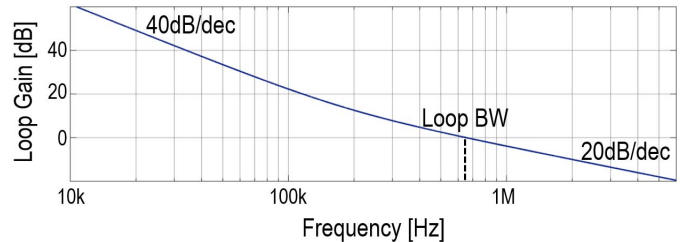


Fig. 9. Loop gain of the type-II EO-PLL.

range to suppress that. For this reason, a charge-pump type-II PLL architecture is employed in this paper. Waveguide connection between the optical elements causes an approximately 20-ns time delay in the loop. To maintain a 70° phase margin with this constant delay in the loop, a bandwidth lower than approximately 700 kHz is chosen. The overall open-loop gain for the EO-PLL is given in Fig. 9.

It is worth mentioning that when designing type-II EO-PLLs, the tuning speed of the laser may also be of significance. The DBR laser used in this paper has a 60-MHz tuning bandwidth, which is far larger than the EO-PLL bandwidth and its effect on the phase margin is negligible. For thermally or mechanically tuned lasers, the tuning bandwidth can be much smaller, in which case its effect on the EO-PLL dynamics must be considered.

B. Maximum Modulation Speed

A higher modulation speed is desired for increasing the gain of the system, which, from (1), is proportional to the modulation slope γ and also for enabling larger throughput. However, by increasing the modulation speed, the error due to nonlinearity will also repeat at a higher rate and the EO-PLL will be less effective in suppressing it. Without using EO-PLL, the nonlinearity and its drift can result in a 65-μm ranging error, which is not acceptable for many applications. For instance, present-day 3D printers can have a depth resolution as good as 20 μm, and to harvest this capability for rapid prototyping, a 3D imager with even better resolution (e.g., sub-10 μm) is required. In addition, in medical applications, such as 3D corneal imaging or 3D vision for robotic microsurgery, a sub-10-μm resolution can enable 3D imaging at cellular level and provide the maximum possible reliability in such applications. Thus, to have any meaningful impact, the feedback loop should be able to suppress the ranging error from 65 μm to less than 10 μm. As shown in Fig. 9, the frequency of the triangular modulation should be less than 125 kHz, for its nonlinearity to be suppressed by 7 times (17 dB) loop gain, which is equivalent to 4-μs single-ramp duration. To maintain some extra margin, in the final design, $T_{ramp} \approx 5.5 \mu\text{s}$ is used. Thus

$$\gamma = \frac{\Delta f_{max}}{T_{ramp}} = \frac{120 \text{ GHz}}{5.5 \mu\text{s}} = 22 \text{ GHz}/\mu\text{s}. \quad (11)$$

From (10), the value of γ is controlled by τ_{MZI} and f_{LO} . A large value for f_{LO} relaxes the phase-margin requirement of the EO-PLL; however, with a fixed γ , it requires a large τ_{MZI} . A longer MZI waveguide has more loss and occupies

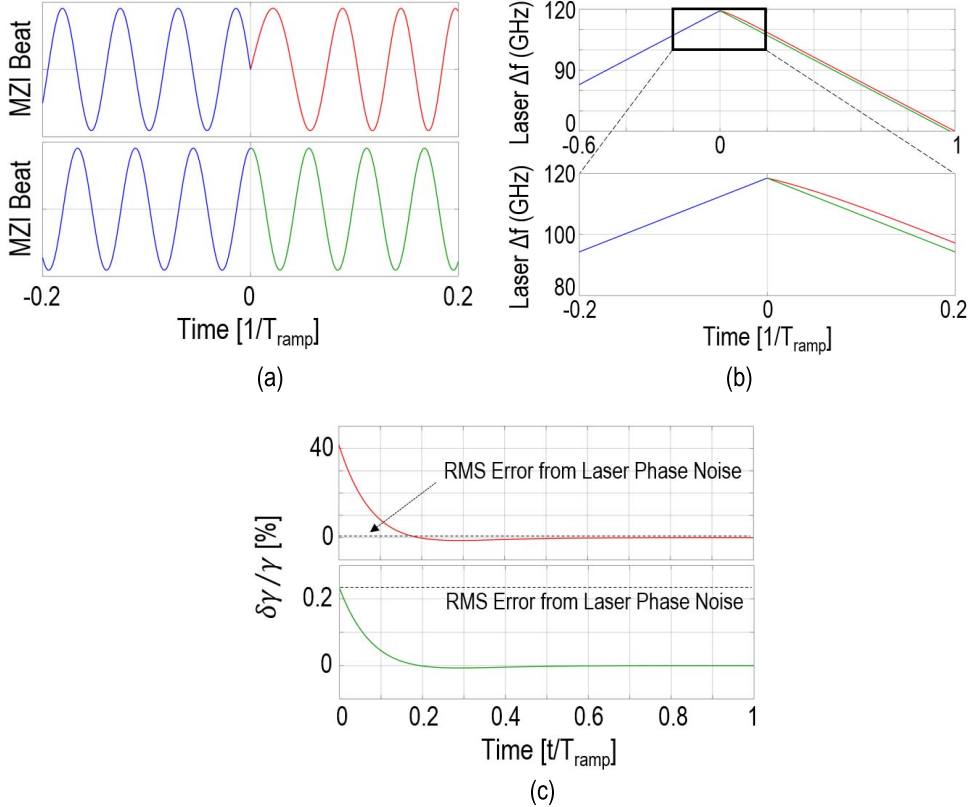


Fig. 10. Effect of switching at zero crossing and peak of the beat signal on the EO-PLL performance. (a) Switching effect on MZI beat signal. (b) Switching effect on the modulation ramp. (c) Normalized switching error in the modulation slope, γ .

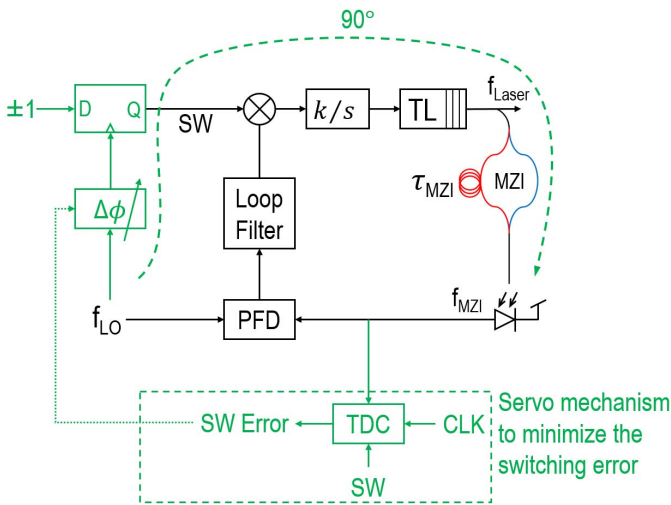


Fig. 11. Architecture of the EO-PLL with gated ramp switching.

larger area. In this design, $\tau_{MZI} = 330$ ps corresponding to 10-cm optical waveguide length on the photonic chip is chosen. With this delay, the resulting LO frequency is 7.2 MHz.

C. Gated Ramp Switching

Switching the direction of the modulation ramp can cause a phase jump in the MZI beat signal. As shown in Fig. 10, the maximum and minimum phase jumps occur when the ramp-switching instant aligns with a zero crossing or peak of the MZI signal, respectively. The phase jump caused by ramp switching forces the EO-PLL out of lock and, as shown

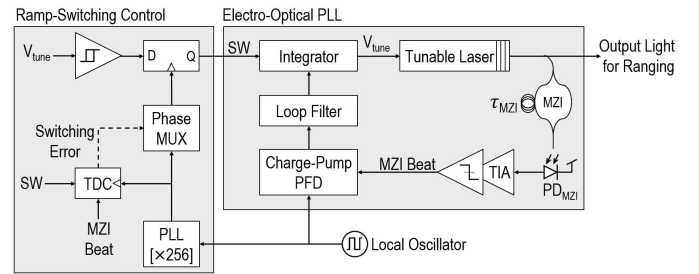


Fig. 12. Detailed block diagram of the EO-PLL with gated ramp switching.

in Fig. 10(b), introduces nonlinearity to the modulation waveform. The normalized error in the modulation slope is shown in Fig. 10(c). In Fig. 10, the green curves correspond to the case with switching close ($\pm 1^\circ$) to a peak of the MZI beat signal, in which case the switching error becomes negligible; hence, a mechanism to align the switching instant with a peak of the MZI beat signal can suppress this error.

Because the LO and MZI beat signals are phase locked, the transition (rising or falling edge) of the LO signal can be used as a reference to gate the switching signal and delay it until the beat signal peak, to minimize the switching error. Such a mechanism is shown in Fig. 11. The phase shift $\Delta\phi$ on the LO edge should be adjusted so that, combined with the parasitic delay from other elements in the signal path, the overall delays sum up to 90° . This adjustment is made in a servo loop by observing the error in the period of the beat signal after each switching instant using a time-to-digital converter (TDC) and setting $\Delta\phi$ to minimize this error.

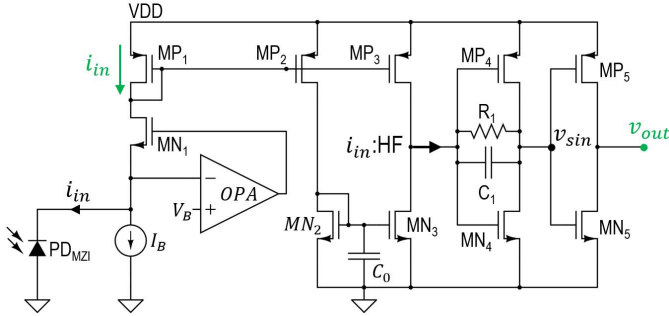


Fig. 13. Circuit schematic of the electronic front end.

D. Design of the EO-PLL Circuit Blocks

A detailed block diagram of the EO-PLL with gated ramp switching is shown in Fig. 12. In this section, the important design considerations for the front-end electronics and the ramp-switching block will be discussed.

1) Front-End Electronics: The photocurrent from the MZI Photodiode (PD_{MZI}) is converted to a square voltage to be applied to the charge-pump PFD. As shown in Fig. 13, this task is accomplished using a transimpedance amplifier (TIA) followed by a voltage limiter. The TIA consisting of a low-impedance input stage implemented by the gm-boosted transistor MN_1 , and the transresistance R_1 amplifies and high-pass filters ($MP/N_{2,3}$) the current to remove the low-frequency baseline variation caused by the laser's intensity fluctuation as a side effect of its frequency tuning. The high-frequency noise is filtered through capacitor C_1 (140 fF) in parallel with R_1 (10 k Ω). An inverter (MP/N_5) matched with the transimpedance stage (MN/P_4) removes the amplitude envelope before the PFD.

The auxiliary MZI employed in the EO-PLL is essentially equivalent to a short-range target with a round-trip-delay of $\tau_{\text{MZI}} = 330$ ps. From (8), and given that the amplitude of the photocurrent at the output of the PD_{MZI} is equal to 10 μA , the current noise density caused by the laser-phase noise is equal to 80 pA $^2/\text{Hz}$. The input-referred noise from the front-end electronics must be kept below this level. The input-referred current noise from MN_1 is suppressed by the gain-boosting amplifier, OPA. The noise from the transistors MN/P_2 is low-pass filtered through the capacitor C_0 ; hence, the input referred current noise is dominated by the transistors $MP_{1,3}$ and MN_3 and the resistor R_1 ; thus, the following is required:

$$g_{m_{n1}} + g_{m_{p1}} + g_{m_{p3}} + \frac{1}{R_1} < 5 \text{ mS.} \quad (12)$$

By choosing the 1/f noise corner frequency below $1/T_{\text{ramp}} = 180$ kHz, its effect on the accumulated phase of the MZI and ranging signals within each modulation period will be negligible as well.

2) Ramp Switching: An implementation of the gated ramp switching is shown in Fig. 12. The pre gated switching signal is generated using a hysteresis comparator that senses the tuning voltage and is designed to toggle and change the integration direction when this voltage crosses the allowed boundaries. The comparator output is gated and applied to the integrator

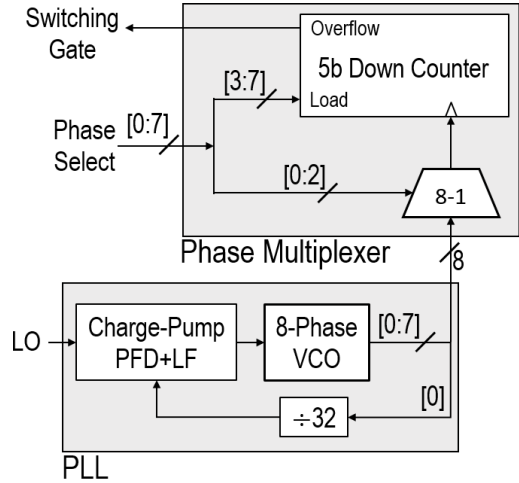


Fig. 14. Architecture of the digitally controlled phase-delay generated for gated ramp switching.

to change the ramp direction at the next peak of the MZI signal.

The gating signal is generated from the LO using a PLL followed by a phase multiplexer. A block diagram of the PLL and phase multiplexer is shown in Fig. 14. The PLL employs a four-stage differential VCO with eight output phases. The frequency of the VCO is set to $32 \times f_{\text{LO}}$; hence, within each LO cycle, there are 256 equally spaced edges that can be selected by the phase-multiplexer to gate the switching signal. The phase multiplexer sets the switching gate by selecting one of the VCO outputs and feeding it to a 5-b free-running counter that generates an overflow after counting down from its loaded input. A TDC uses the output of the PLL as an eight-phase reference clock and measures the error in the period of the beat signal after each switching instant. The phase-select bits of the phase-multiplexer are then set to minimize the switching error.

V. EO-PLL VERIFICATION AND IMPLEMENTATION

One of the challenges to implementing integrated electronic-photonic circuits is their verification. There are well-established simulation tools for electronic circuits; photonic circuits can be modeled and simulated using similar tools (e.g., modeling in Verilog-A and simulation with Spectre). In this paper, the time scale for accurate simulation of the electronic circuits can be milliseconds; however, the central frequency of the optical fields is approximately 200 THz. The time-domain simulation of a large-scale network with such high-frequency signals for a time duration of milliseconds can take days or even weeks. For this reason, the photonic signals and elements are modeled and simulated in amplitude and phase/frequency domains. Imperfections, such as laser tuning characteristic, phase noise, the frequency dependence of its intensity, and MZI loss, are included in the models.

All of the electronic and photonic circuits in the architecture of the EO-PLL shown in Fig. 12 are integrated on a chip-scale platform, except for the tunable laser. The electronic circuits are fabricated in 0.18- μm CMOS technology, and the MZI and photodiode are implemented on a silicon-photonic chip. Photomicrographs of the chips are shown in Fig. 15. Both of

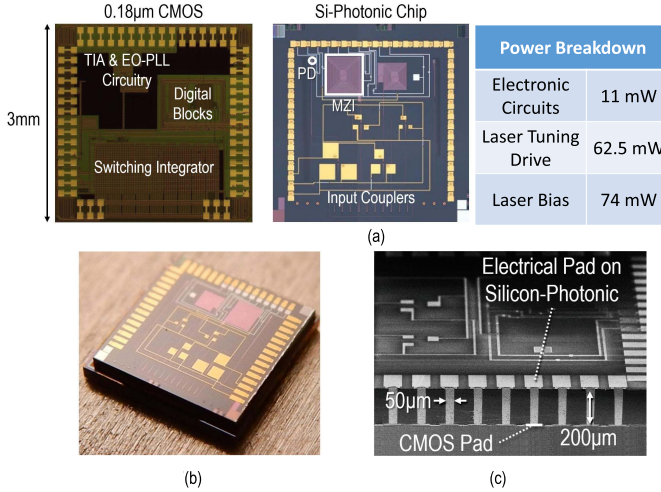


Fig. 15. EO-PLL implemented on a heterogeneously integrated electronic-photonic chip. (a) Photograph of the CMOS and silicon-photonic chips and power consumption breakdown. (b) Photograph of the integrated electronic-photonic stack. (c) Tilted SEM of the integrated stack diced along the TSVs.

the chips occupy $3 \times 3 \text{ mm}^2$ and are pitch matched for stack integration with through-silicon-vias (TSVs). A photograph of the integrated stack and a tilted SEM of the stacked chips diced at the position of the TSVs are shown in Fig. 15(b) and (c), respectively.

VI. EXPERIMENTAL RESULTS

This section presents the measurement results for the EO-PLL's performance in linearizing the laser frequency modulation, as well as its application for ranging and 3D microimaging.

A. EO-PLL Performance

The performance of the EO-PLL is quantified by measuring the error on the modulation slope, γ . The frequency of the MZI beat signal is proportional to γ and is measured to determine its value. For this purpose, the cycle-to-cycle frequency of the square-wave voltage at the TIA output on the CMOS chip is recorded. The plot of the normalized error in γ versus a single modulation ramp for three experiments is shown in Fig. 16. The top panel corresponds to the experiment with open-loop modulation of the laser's frequency. The middle panel is measured when using the EO-PLL without gated ramp switching; the large error in the beginning of the period is caused by the switching at an arbitrary phase of the MZI signal. The bottom panel shows the performance of the EO-PLL with gated ramp switching. The error in this case is dominated by the contribution of the laser's phase noise and the error components due to laser's tuning nonlinearity, its drift, and ramp switching are negligible.

B. Ranging and 3D Microimaging Applications

Improved precision of the laser frequency-modulation slope enables ranging with precision close to the theoretical curve derived in Section II. Fig. 17 shows the ranging setup. The laser light power is split into two paths; one path is directed

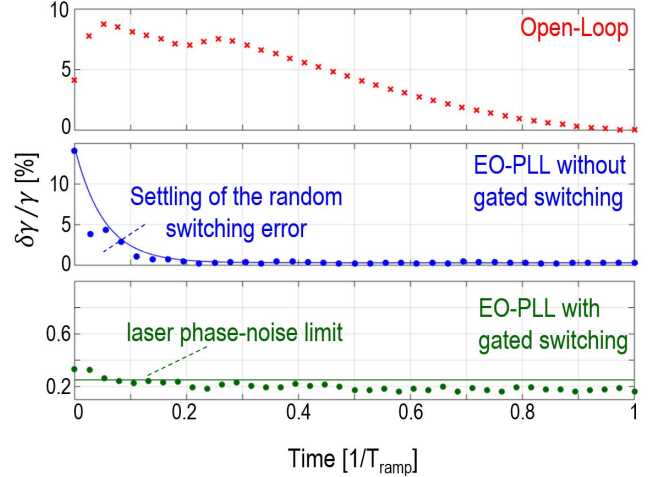


Fig. 16. Precision of the laser frequency-modulation slope (γ) under different conditions.

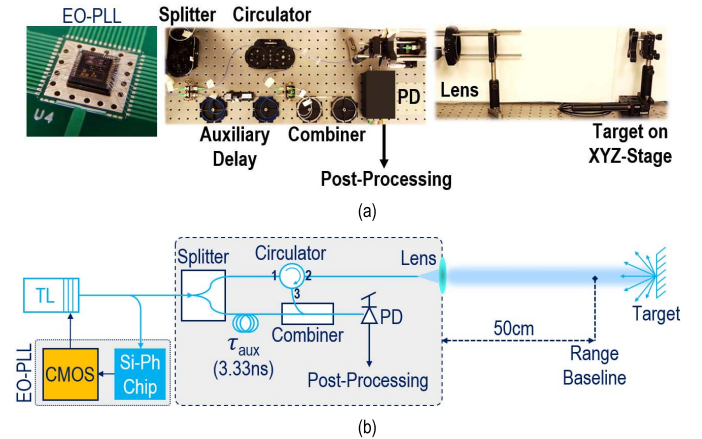


Fig. 17. Experimental setup for ranging. (a) Photograph. (b) Schematic.

to the on-chip MZI to monitor and regulate the frequency-modulation slope with the EO-PLL circuitry and the other path is used for ranging. The frequency of the ranging signal is proportional to the difference between the target distance and the length of the local branch, $2R - c \cdot \tau_0$. This frequency is extracted and normalized to the MZI beat frequency in postprocessing steps to determine the range

$$\frac{f_{\text{MZI}}}{l_{\text{MZI}}} = \frac{f_R}{2R - c \cdot \tau_0} \Rightarrow R = \frac{f_R}{f_{\text{MZI}}} \cdot l_{\text{MZI}} + \frac{c \cdot \tau_0}{2}. \quad (13)$$

With this ratio-metric measurement, the optical length difference of the on-chip MZI branches can be used as the length unit for the target range measurement. Furthermore, because the slow drift of f_{LO} has proportional effect on f_R and f_{MZI} , the ratio-metric measurement can relax the requirements for the close-to-carrier phase noise of the LO.

It must be noted that the effect of the laser phase noise on the ranging error is a function of the path-length difference, $2R - c \cdot \tau_0$ and will be minimum when the path-length-difference is equal to zero. In the setup shown in Fig. 17, τ_0 is set to 3.3 ns; hence, the ranging error due to the laser's phase noise would be minimum at a range baseline of 50 cm.

The ranging error is measured both for open-loop laser modulation and with EO-PLL. A target with a return loss of

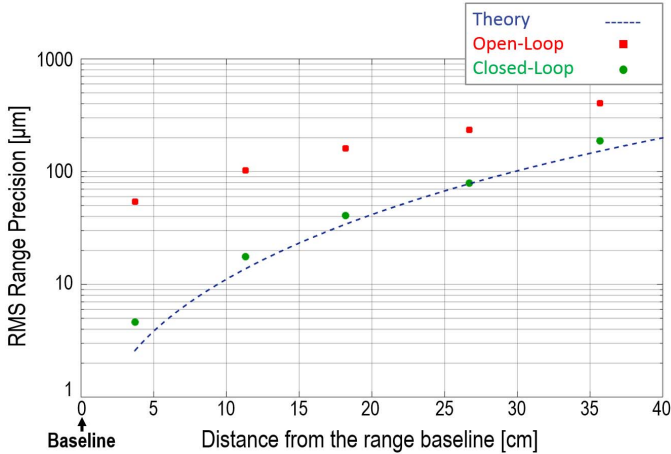


Fig. 18. Ranging precision versus distance from the range baseline.

approximately 5 dB is incrementally moved away from the range baseline and at each point 14 ranging measurements each with the duration of a single modulation ramp ($5.5 \mu\text{s}$) are performed. The standard deviation of these measurements versus distance from the range baseline is shown in Fig. 18. The precision of the measurement with open-loop modulation is limited by the error on the modulation slope, γ . When using the EO-PLL, the error in the modulation slope is suppressed to a negligible level and the standard deviation of the measurements is reasonably close to the expected theoretical curve.

It is worth to mention that the motion of the target or vibration of its surface can cause Doppler shift in the reflected light frequency, which in turn, changes the measured interference frequency f_R . The change in f_R has the same absolute value but opposite sign for the up and down ramps, which can be used to infer the object speed. For instance, using the DBR laser with 1530-nm wavelength and for an object moving away from the lidar aperture at the speed of 1 m/s, the frequency f_R will increase by approximately 650 kHz during the up ramp and will decrease by the same amount during the down ramp. Therefore, a measured difference of 1.3 MHz between the values of f_R during up- and down ramps, while the laser beam points at the same direction, can be interpreted as 1-m/s object speed.

The same setup shown in Fig. 19 is also used for 3D imaging. For this purpose, the target is stepped in the XY plane, and the distance to each point of the object's surface is recorded in a point cloud matrix. Fig. 19(b) shows a photograph and 3D image of a miniature gear, acquired with this technique. The gear is at 40-cm distance from the lens. With 100- μs data length per measurement, the precision is 11 μm , which appears as a roughness on the object's surface.

VII. CONCLUSION

A comparison between the results of this paper and other ranging and 3D imaging techniques is given in Table I. The integrated EO-PLL presented in this paper enables 3D imaging with micrometer-level precision in a chip-scale platform. In addition to numerous applications in

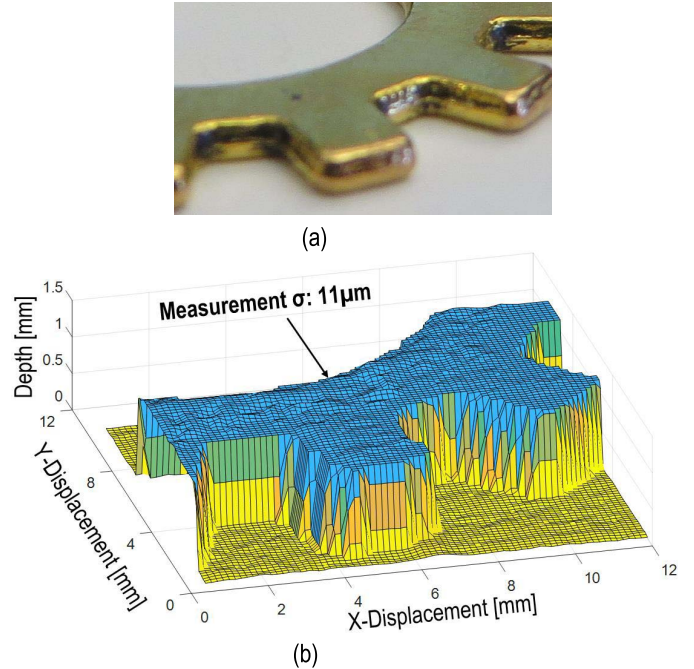


Fig. 19. (a) Photograph and (b) 3D image of a miniature gear acquired using the measurement setup of Fig. 17.

TABLE I
PERFORMANCE COMPARISON TO OTHER 3D IMAGING TECHNIQUES

	2014 [9]	2013 [10]	2014 [12]	2015 [17]	This work
Method	Ultrasonic	Radar	T.o.F Lidar	FM Lidar	FM Lidar
Technology	ALN pMUT 0.18 μm CMOS	65nm CMOS	0.11 μm CIS	Si-Ph	180nm CMOS 250nm Si-Ph
Depth-Precision (σ)	410 μm	1000 μm	300 μm	15 μm	8μm
XY Res. @ 50cm	12.9cm	2.3cm	Not Specified	50um	250um
Mod. BW /Mod. λ	7kHz /48mm	0.57GHz /520mm	28GHz /10.7mm	3.8GHz /78.9mm	122GHz /2.4mm
Range	1m	2m	0.032m	0.5m	1.4m
Emitted Power	-12dBm	-5dBm	Not Specified	20.8dBm	10dBm
Meas. Rate	0.17kP/s	Not Specified	152kP/s	32kP/s	180kP/s

manufacturing industries, this paper enables further application of 3D microimaging in a wider range of fields, such as miniature 3D imagers for robotic microsurgery devices and corneal imaging for contact lens fitting in medical fields, and high-fidelity 3D copy machines for rapid prototyping.

The miniaturization also has favorable effects on the performance of the system. By reducing the length of the electrical wires and optical fibers in the feedback path, the dynamics of the EO-PLL can be improved to suppress the higher frequency errors. Furthermore, close integration of the electronic circuits with photonic devices enables sophisticated control mechanisms, such as the proposed gated-switching technique.

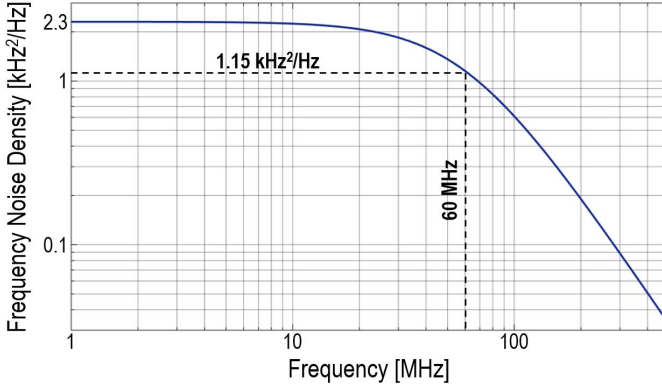


Fig. 20. Frequency noise spectrum of the DBR laser dominated by the tuning process.

APPENDIX

PHOTOCURRENT SPECTRUM IN FMCW LIDAR WITH COLORED FREQUENCY-NOISE SPECTRUM

In general, spontaneous emission is the dominant source of the frequency noise in fixed-wavelength lasers and can be modeled with a white spectrum for the laser frequency. In tunable lasers, the frequency noise has an additional component from the tuning process for which the spectrum is shaped by the tuning transfer function. Tuning processes based on carrier injection, thermal expansion, or thermo-optic effect exhibit the first-order transfer functions. The bandwidth of the tuning transfer function for thermally tuned lasers is usually limited from the kHz to MHz range, whereas with carrier injection, multiple tens of MHz are achievable. In MEMS-tunable lasers, with one dominant mechanical resonance mode for the MEMS mirror, the tuning transfer function has a second-order shape with a bandwidth defined by the mechanical design of the mirror.

In this analysis, the spectrum of the photocurrent in an FMCW lidar employing a tunable laser is derived. It is assumed that the tuning has a first-order transfer function with a bandwidth of ω_p . The frequency noise of the laser is assumed to have a dc level of f_n^2 Hz²/Hz, dominated by the tuning noise and the effect of the spontaneous emission is considered negligible.

Assuming a linear frequency modulation for the tunable laser, its electric field can be written in the following form:

$$e(t) = e_0 \cdot \cos \left(\omega_0 t + \frac{\gamma t^2}{2} + \varphi_n(t) \right) \quad (14)$$

where e_0 is the amplitude of the electric field, ω_0 is the central frequency of the laser, γ is the modulation slope, and $\varphi_n(t)$ is the phase noise. For a round-trip delay of τ_R , the photocurrent at the coherent receiver will have the following waveform:

$$i(t) = i_0 \cdot \cos(\varphi_0 + \gamma \tau_R t + \Delta\varphi_n(\tau_R, t)) \quad (15)$$

where φ_0 is a constant phase component equal to $\omega_0 \tau_R + \gamma ((\tau_R^2)/2)$, $\gamma \tau_R$ is the frequency of the beat signal, and $\Delta\varphi_n(\tau_R, t)$ is the phase noise difference between the two interfering light fields

$$\Delta\varphi_n(\tau_R, t) = \varphi_n(t + \tau_R) - \varphi_n(t). \quad (16)$$

From [18], the autocorrelation of the photocurrent in (15) can be written in the following form:

$$R_i(u) = \frac{i_0^2}{2} \cos(\gamma \tau_R \cdot u) e^{-\sigma_\theta^2(\tau_R, u)} \quad (17)$$

where the term $\sigma_\theta^2(\tau_R, u)$ is the contribution of the laser's phase noise φ_n and can be written as

$$\begin{aligned} \sigma_\theta^2(\tau_R, u) &= 2\sigma_{\Delta\varphi_n}^2(\tau_R) + 2\sigma_{\Delta\varphi_n}^2(u) - \sigma_{\Delta\varphi_n}^2(u + \tau_R) \\ &\quad - \sigma_{\Delta\varphi_n}^2(u - \tau_R) \end{aligned} \quad (18)$$

with $\sigma_{\Delta\varphi_n}^2(a)$ defined as $\langle |\Delta\varphi_n(a, t)|^2 \rangle$. In [18], the value of $\sigma_{\Delta\varphi_n}^2(a)$ was replaced with $\Delta\omega|a|$, which is the result of assuming a white frequency noise spectrum. In this paper, $\sigma_{\Delta\varphi_n}^2(a)$ will be calculated without this assumption and the result from (17) and (18) will be used to find the power spectral density of the photocurrent. For the laser with frequency noise spectrum shown in Fig. 20, the phase noise spectrum can be written in the following form:

$$S_{\varphi_n}(\omega) = \frac{1}{\omega^2} \cdot \frac{4\pi^2 \cdot f_n^2}{1 + (\omega/\omega_p)^2} [\text{rad}^2/\text{Hz}]. \quad (19)$$

The transfer function from the laser phase to $\Delta\varphi_n(a)$ is the subtraction of the two copies of φ_n by delay a , which can be written in the form of $1 - e^{-j\omega a}$. Applying this transfer function to (19), results in the spectrum of $\Delta\varphi_n(a)$

$$\begin{aligned} S_{\Delta\varphi_n(a)}(\omega) &= |1 - e^{-j\omega a}|^2 \cdot \frac{1}{\omega^2} \cdot \frac{4\pi^2 \cdot f_n^2}{1 + (\omega/\omega_p)^2} \\ &= \text{sinc}^2(\omega a/2) \cdot \frac{1}{\omega^2} \cdot \frac{4\pi^2 \cdot a^2 \cdot f_n^2}{1 + (\omega/\omega_p)^2} [\text{rad}^2/\text{Hz}]. \end{aligned} \quad (20)$$

To find $\sigma_{\Delta\varphi_n}^2(a)$, this spectrum should be integrated over all frequencies, resulting in the following:

$$\sigma_{\Delta\varphi_n}^2(a) = \frac{4\pi^2 f_n^2}{\omega_p} [a \cdot \omega_p - 1 + \cosh(a \cdot \omega_p) - \sinh(a \cdot \omega_p)]. \quad (21)$$

For the laser used in this paper with $f_n^2 = 2.3 \times 10^6$ Hz²/Hz and $\omega_p = 2\pi \times 60$ Mrad/s, the plot of $\sigma_{\Delta\varphi_n}^2(a)$ is shown in Fig. 21. The graph based on the assumption of a white frequency noise spectrum is also shown on the same figure for comparison. As can be seen on this plot, the effect of a limited frequency noise bandwidth on $\sigma_{\Delta\varphi_n}^2(a)$ is significant, particularly for the values of $|a| \ll 1/\omega_p$.

The result of (21) can now be combined with (17) and (18) to find the autocorrelation function and, consequently, the spectrum of the photocurrent. While this can be done using the accurate form of (21) followed by numerical techniques, it is intuitive to use a simplified approximation for this equation and find a closed-form solution for the photocurrent spectrum. Equation (21) can be divided into two different regions; for small values of $a \cdot \omega_p$, the hyperbolic functions can be expanded in the first few terms of their Taylor series; for large values of $a \cdot \omega_p$, it can be shown that the value of

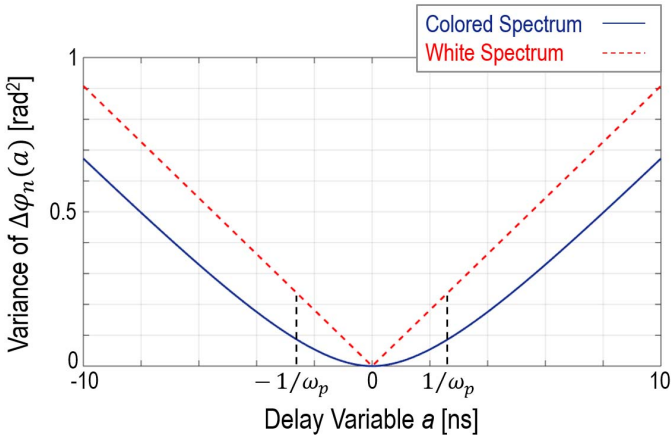


Fig. 21. Plot of $\sigma_{\Delta\phi_n}^2(a)$ versus delay variable “ a ,” for a tunable laser with band-limited frequency noise. The plot with the assumption of white frequency noise is also provided for comparison.

$\cosh(a \cdot \omega_p) - \sinh(a \cdot \omega_p)$ approaches zero exponentially. Therefore, (21) can be approximated in the following form:

$$\sigma_{\Delta\phi_n}^2(a) = \frac{4\pi^2 f_n^2}{\omega_p} \begin{cases} \frac{(|a| \cdot \omega_p)^2}{2} - \frac{(|a| \cdot \omega_p)^3}{6}, & |a| \leq \omega_p^{-1} \\ \frac{|a| \cdot \omega_p - 2/3}{|a| \cdot \omega_p - 2/3}, & |a| > \omega_p^{-1} \end{cases} \quad (22)$$

where the constant for the large values of $a \cdot \omega_p$ has been adjusted ($1 \rightarrow 2/3$) to maintain continuity at $a \cdot \omega_p = 1$. Using this approximation and for the values of $\tau_R \leq \omega_p^{-1}$, (18) can be evaluated as

$$\sigma_{\Delta\phi_n}^2(a) = \frac{4}{\zeta_R} \begin{cases} |u| - \frac{\tau_R}{3}, & |u| \leq \omega_p^{-1} \\ \frac{1}{\omega_p} - \frac{\tau_R}{3}, & |a| > \omega_p^{-1} \end{cases} \quad (23)$$

where $\zeta_R = (\pi^2 f_n^2 \omega_p^2 \tau_R^2)^{-1}$ is defined for algebraic simplicity as a function of the laser parameters and the target distance. This result combined with (17) determines the autocorrelation function. The Fourier transform of this function around the carrier ($f = \gamma \cdot \tau_R$) is the spectral density of the photocurrent

$$S_i(\omega) = \frac{i_0^2}{2} \left\{ e^{\frac{-2}{\zeta_R \cdot \omega_p}} \cdot \delta(\omega) + \frac{\zeta_R}{1 + (\zeta_R \omega_p / 2)^2} \cdot \left[1 - e^{\frac{-2}{\zeta_R \cdot \omega_p}} \cdot \left(\cos\left(\frac{\omega}{\omega_p}\right) + \frac{1}{\zeta_R \cdot \omega} \cdot \sin\left(\frac{\omega}{\omega_p}\right) \right) \right] \right\}. \quad (24)$$

The first term is a Delta function that contains the signal information, and the second term is the spectral density of the noise. It is worth noting two important points in this equation. First, unlike the analysis based on the assumption of white frequency spectrum for the laser [18], the spectral density of the photocurrent for $\tau_R \leq \omega_p^{-1}$ is heavily dependent on the bandwidth of the laser’s frequency noise spectrum, ω_p . For thermally or mechanically tuned lasers, in which the tuning bandwidth is smaller than the bandwidth of the DBR laser used in this paper, the effect of the colored noise spectrum will be even more pronounced. For MEMS tunable lasers, the frequency noise spectrum will have a second-order roll-off and

may include peaking in its transfer function, which should be carefully considered when evaluating $\sigma_{\Delta\phi_n}^2(a)$ in (21). Second, the amplitude of the signal drops exponentially as a function of τ_R^2 . Whereas, based on the assumption of a white frequency spectrum, the degradation of the signal with increasing target distance would occur as an exponential function of τ_R .

In practice, because of the limited duration of the modulation ramp, only time-windowed versions of this signal can be measured. To account for this effect, the resulting spectrum should be convolved with a sinc function as shown in the following:

$$S_i(\omega) = \frac{i_0^2}{2} \left\{ e^{\frac{-2}{\zeta_R \cdot \omega_p}} \cdot \text{sinc}^2\left(\frac{T_{\text{ramp}} \cdot \omega}{2}\right) + \frac{\zeta_R}{1 + (\zeta_R \omega_p / 2)^2} \cdot \left[1 - e^{\frac{-2}{\zeta_R \cdot \omega_p}} \cdot \left(\cos\left(\frac{\omega}{\omega_p}\right) + \frac{1}{\zeta_R \cdot \omega} \cdot \sin\left(\frac{\omega}{\omega_p}\right) \right) \right] \right\}. \quad (25)$$

Typically, in an FMCW lidar with linear frequency modulation, $T_{\text{ramp}} \gg (1/(\omega_p))$ and, as a result, the function $\text{sinc}^2((T_{\text{ramp}}\omega)/2)$ has a much narrower spectral width than the noise and can be considered as a Delta function when being convolved to it. Thus, the effect of windowing on the noise spectrum can be neglected.

ACKNOWLEDGMENT

The authors would like to thank the DARPA’s Diverse Accessible Heterogeneous Integration Program. They would also like to thank the TSMC University Shuttle Program for CMOS chip fabrication, the Marvell Nanofabrication Laboratory at the University of California at Berkeley, for the fabrication of the silicon-photonic chips, the Berkeley Sensor and Actuator Center, and the UC Berkeley SwarmLab for their continuous support.

REFERENCES

- [1] C. Wheatstone, “Contributions to the physiology of vision,” *Philos. Trans. Roy. Soc. London*, vol. 128, pp. 371–394, Jan. 1838.
- [2] A. Darabiha, J. Rose, and J. W. Maclean, “Video-rate stereo depth measurement on programmable hardware,” in *Proc. IEEE Comput. Soc. Conf. Comput. Vis. Pattern Recognit.*, vol. 1, Jun. 2003, pp. 203–210.
- [3] P. M. Will and K. S. Pennington, “Grid coding: A preprocessing technique for robot and machine vision,” *Artif. Intell.*, vol. 2, nos. 3–4, pp. 319–329, 1971.
- [4] M. D. Altschuler, J. Taboada, and B. R. Altschuler, “Measuring surfaces space-coded by a laser-projected dot matrix,” *Proc. SPIE*, vol. 182, pp. 187–191, Oct. 1979.
- [5] D. Scharstein *et al.*, “High-accuracy stereo depth maps using structured light,” in *Proc. IEEE Comput. Soc. Conf. Comput. Vis. Pattern Recognit.*, vol. 1, Jun. 2003, pp. 195–202.
- [6] P. Grossman, “Depth from focus,” *Pattern Recognit. Lett.*, vol. 5, no. 1, pp. 63–69, 1987.
- [7] A. P. Pentland, “A new sense for depth of field,” *IEEE Trans. Pattern Anal. Mach. Intell.*, vol. PAMI-9, no. 4, pp. 523–531, Apr. 1987.
- [8] S. Hiura and T. Matsuyama, “Depth measurement by the multi-focus camera,” in *Proc. IEEE Comput. Soc. Conf. Comput. Vis. Pattern Recognit.*, Jun. 1998, pp. 953–959.
- [9] R. J. Przybyla, H. Y. Tang, A. Guedes, S. E. Shelton, D. A. Horsley, and B. E. Boser, “3D ultrasonic rangefinder on a chip,” *IEEE J. Solid-State Circuits*, vol. 50, no. 1, pp. 320–334, Jan. 2015.
- [10] P.-N. Chen, P.-J. Peng, C. Kao, Y.-L. Chen, and J. Lee, “A 94 GHz 3D-image radar engine with 4TX/4RX beamforming scan technique in 65 nm CMOS,” in *ISSCC Dig. Tech. Papers*, Feb. 2013, pp. 146–147.

- [11] R. A. Lewis and A. R. Johnston, "A scanning laser rangefinder for a robotic vehicle," in *Proc. 5th Int. Joint Conf. Artif. Intell.*, vol. 2, 1977, pp. 762–768.
- [12] K. Yasutomi, T. Usui, S.-M. Han, T. Takasawa, K. Kagawa, and S. Kawahito, "A 0.3mm-resolution time-of-flight CMOS range imager with column-gating clock-skew calibration," in *ISSCC Dig. Tech. Papers*, Feb. 2014, pp. 132–133.
- [13] A. Olsson and C. L. Tang, "Dynamic interferometry techniques for optical path length measurements," *Appl. Opt.*, vol. 20, no. 20, pp. 3503–3507, 1981.
- [14] E. C. Burrows and K.-Y. Liou, "High resolution laser LIDAR utilising two-section distributed feedback semiconductor laser as a coherent source," *Electron. Lett.*, vol. 26, no. 9, pp. 577–579, 1990.
- [15] A. Dieckmann, "FMCW-LIDAR with tunable twin-guide laser diode," *Electron. Lett.*, vol. 30, no. 4, pp. 308–309, Feb. 1994.
- [16] N. Satyan, A. Vasilyev, G. Rakuljic, V. Leyva, and A. Yariv, "Precise control of broadband frequency chirps using optoelectronic feedback," *Opt. Exp.*, vol. 17, no. 18, pp. 15991–15999, Aug. 2009.
- [17] F. Aflatouni, B. Abiri, A. Rekhi, and A. Hajimiri, "Nanophotonic coherent imager," *Opt. Exp.*, vol. 23, no. 4, pp. 5117–5125, 2015.
- [18] A. Vasilyev, "The optoelectronic swept-frequency laser and its applications in ranging, three-dimensional imaging, and coherent beam combining of chirped-seed amplifiers," Ph.D. dissertation, Dept. Elect. Eng., Caltech Univ., Pasadena, CA, USA, 2014.
- [19] Y. Matsui *et al.*, "Transceiver for NG-PON2: Wavelength tunability for burst mode TWDM and point-to-point WDM," in *Opt. Fiber Commun. Conf. Tech. Dig.*, 2016, p. Tu2C-1.



Behnam Behroozpour (S'12–M'16) received the B.Sc. degree from the Sharif University of Technology, Tehran, Iran, in 2010, the M.Sc. degree from the University of Twente, Enschede, The Netherlands, in 2012, and the Ph.D. degree from the University of California at Berkeley, Berkeley, CA, USA, in 2016.

He is currently a Research Engineer with the Bosch Research and Technology Center, Palo Alto, CA, USA. His current research interests include analog and mixed-signal integrated circuits, photonic integrated circuits, MEMS, LIDAR, and 3D imaging technologies.



Phillip A. M. Sandborn received the B.Sc. degree in electrical engineering and mathematics from the University of Maryland, College Park, MD, USA, in 2012. He is currently pursuing the Ph.D. degree in electrical engineering with the University of California at Berkeley, Berkeley, CA, USA.

His current research interests include 3D imaging using LIDAR, optical phase-locked loops, optical packaging, and noise-limited performance of optical systems.



Niels Quack (S'05–M'11–SM'15) received the M.Sc. degree from the Ecole Polytechnique Fédérale de Lausanne (EPFL), Lausanne, Switzerland, in 2005, and the Dr.Sc. degree from the Eidgenössische Technische Hochschule Zürich, Zürich, Switzerland, in 2010.

From 2011 to 2015, he was a Post-Doctoral Researcher and a Visiting Scholar with the Integrated Photonics Laboratory, Berkeley Sensor and Actuator Center, University of California at Berkeley, Berkeley, CA, USA. From 2014 to 2015,

he was a Senior MEMS Engineer with Sercalo Microtechnology Ltd., Neuchâtel, Switzerland. He is currently a Swiss National Science Foundation Funded Professor with EPFL. He has authored or co-authored over 30 papers in leading technical journals and conferences. His current research interests include MEMS, optical MEMS, tunable optical microsystems, optomechanical oscillators, silicon photonics, heterogeneous integration, LIDAR, and diamond photonics.



Tae-Joon Seok (S'08–M'14) received the B.S. degree in electrical engineering from Seoul National University, Seoul, South Korea, in 2007, and the Ph.D. degree in electrical engineering and computer sciences from the University of California at Berkeley, Berkeley, CA, USA, in 2012.

He has been a Post-Doctoral Scholar with the University of California at Berkeley since 2013. He has authored over 40 papers in leading technical journals and conferences. His current research interests include optoelectronics, nanophotonics, plasmonics, and silicon photonics.

Dr. Seok is currently a member of the Optical Society (OSA). He received the 2015 Tingye Li Innovation Prize from OSA and the Bronze Medal of 2015 Collegiate Inventors Competition sponsored by the United States Patent and Trademark Office.



Yasuhiro Matsui received the bachelor's degree in physics from Kyoto University, Kyoto, Japan, and the Ph.D. degree from The University of Tokyo, Tokyo, Japan, in 2000.

He joined the Oki Electric Research Laboratory, Tokyo, Japan, in 1988, where he was involved in high-speed directly modulated lasers (DMLs), narrow-linewidth DBR lasers, terahertz mode-locked lasers, electroabsorption modulators, and high-power lasers. From 1996 to 2000, he conducted research with the Femtosecond Technology Research Association,

Tsukuba, Japan, where he demonstrated sub-100-fs tunable Raman-soliton pulse generation from DMLs. In 2000, he joined CoreTek (acquired by Nortel Networks in 2000), Fredericksburg, VA, USA, where he was involved in polarization control of an MEMS-tunable VCSEL based on the spinflip model. In 2002, he co-founded AZNA, and co-invented the chirp-managed directly modulated laser. He is also an Inventor of thermally tunable narrow linewidth lasers utilizing an air-gap suspended waveguide. After the acquisition of AZNA by Finisar Corporation in 2007, he has been involved in developing high-speed Al-BH DFB and short-cavity DR lasers at 1300 nm and high-power tunable DBR lasers for EPON and NGPON2 applications. He has authored over 100 papers. He holds numerous patents in the U.S. and Japan.



Ming C. Wu (F'02) received the B.S. degree in electrical engineering from National Taiwan University, Taipei, Taiwan, and the M.S. and Ph.D. degrees in electrical engineering and computer sciences from the University of California at Berkeley, Berkeley, CA, USA, in 1986 and 1988, respectively.

From 1988 to 1992, he was a Technical Staff Member with AT&T Bell Laboratories, Murray Hill, NJ, USA. From 1992 to 2004, he was a Professor of Electrical Engineering with the University of California at Los Angeles, Los Angeles, CA, USA. He has been a Faculty Member at Berkeley since 2004. He is currently a Nortel Distinguished Professor of Electrical Engineering and Computer Sciences with the University of California at Berkeley, where he is also a Co-Director of the Berkeley Sensor and Actuator Center and a Faculty Director of UC Berkeley Marvell Nanolab. He has authored eight book chapters and over 500 papers in journals and conferences. He holds 23 U.S. patents. His current research interests include semiconductor optoelectronics, nanophotonics, MEMS, MOEMS, and optofluidics.

Dr. Wu was a Packard Foundation Fellow from 1992 to 1997. He received the 2007 Paul F. Forman Engineering Excellence Award from the Optical Society of America and the 2016 William Streifer Award from the IEEE Photonics Society.



Bernhard E. Boser (F'03) received the Ph.D. degree from Stanford University, Stanford, CA, USA, in 1988.

He was a Member of Technical Staff at Bell Laboratories. In 1992, he joined the Faculty of the EECS Department, UC Berkeley, Berkeley, CA, USA. He is currently a co-founder of SiTime, Santa Clara, CA, USA, and Chirp Microsystems, Berkeley, CA, USA. His current research interests include analog and mixed signal circuits, with special emphasis on ADCs and micromechanical sensors and actuators.

Dr. Boser served as the President of the Solid-State Circuits Society and on the program committees of ISSCC, VLSI Symposium, and Transducers. He also served as the Editor-in-Chief of the IEEE JOURNAL OF SOLID-STATE CIRCUITS.